JOINT INSTITUTE FOR NUCLEAR RESEARCH

Frank Laboratory of Neutron Physics

FINAL REPORT ON THE INTEREST PROGRAMME

3D imaging with neutrons

Supervisor:

Ivan Zel, Ph.D.

Student:

Merell Lystra Ledesma Recta, University of Debrecen

Participation period:

February 14 – March 25, Wave 6

Dubna, 2022

Abstract

Because neutrons have no charge, they can interact with matter greatly, making them a good source for non-destructive testing. Consequently, visualization of the internal structure becomes more accurate paving way for better analysis and diagnosis.

This study introduced me to the tedious world of image processing and challenged me to analyze the composition of a heterogenous rock sample using computing software to produce the desired 3D image. Two of the most common reconstruction algorithms were used in the reconstruction and post-processing stages.

The comparison of the calculated neutron attenuation coefficient helped us qualitatively determine the iron-rich phase and quartz-rich phase of the heterogenous rock sample as well as its relative volume phases.

1. Introduction

With a promising number of 220 operational research reactors around the globe, in which 66 of them are utilized for neutron radiography, the growing interest for the non-destructive imaging technique using a neutron source is evident in the years to come.[8]

Neutrons are electrically neutral subatomic particles which mean that they can deeply penetrate a sample material and interact with both heavy and light elements. Because it possesses no charge, there is no Coulomb barrier to overcome resulting in a close contact with the nuclei—which is not the case for x-rays.[9] In turn, this neutron-matter interaction yields a large difference in scattering that gives a more distinguishable result after image reconstruction.

In archeological studies, the determination of the degradation degree provides further insights into the original internal structure of an object and a key component for the restoration or conservation of it. The analysis of ancient coins by neutron tomography (Kichanov et al., 2017) revealed not only the irregularity on the surface in connection with the patina penetration but also the preserved regions covered by the corrosion layer.

The high sensitivity of neutrons to light atoms such as hydrogen broadens the application of neutron tomography to organic materials (Cleveland et al., 2008). Using this technique, it became possible to identify the anatomical features of a corn kernel and determine infected kernels due to a lower neutron attenuation in scutellum and embryo regions as a result of a decreased hydrogen concentration in the presence of a fungal degradation.

Another non-destructive imaging technique is X-ray tomography that has been widely used in the medical field. But certain drawbacks limit the quality of produced images, making way for neutron tomography as a better and powerful tool in nondestructive analysis particularly in materials with structural inhomogeneity and are rare by nature e.g., pallasites.[5]

Neutron imaging formation applies the principles of the Beer-Lambert Law wherein, depending on the attenuation of the elements in a material, some of the neutrons are absorbed while others are scattered. The measured intensity after the neutron source passes through the sample is best illustrated in the mathematical expression:

$$I = I_0 \exp\left(-\int \mu(x)dx\right)$$

where I is the measured intensity, I_o is the incident beam intensity and μ is the linear attenuation coefficient.

In order to create 2D or 3D images of the internal structure, it is necessary to reconstruct the set of projected 1D images by applying the Fourier slice theorem. This theorem relates the 2D Fourier transform of an image with the Fourier transform of the 1D projections. A number of reconstruction methods are available but the most common are the Filter Back Projection (FBP) and the Simultaneous Iterative Reconstructive Technique (SIRT), both of which are presented in this study.

FBP is a fast and direct method to generate computed tomography images. This algorithm consists of two steps: filtering the data and performing back projection as illustrated in the mathematical expression below.

$$\mu(x,y) = \int_0^\pi \int_0^\infty s_\theta(k)|k|e^{2\pi i k t} \, dk \, d\theta$$

$$\mu(x,y) = \int_0^\pi [Q_\theta(k)] \, d\theta$$

where $|k|$ is the ideal Ramp filter, $Q_\theta(k)$ is the filtered projection and the integration over $d\theta$ is the back projection.

However, this reconstruction method faces another challenge in image analysis. Specifically, it becomes problematic to utilize this algorithm when projections were taken at angles with a non-uniform step or there is a lack in projections.

When tomography involves the use of microwaves or ultrasound, energy propagation is no longer modeled as straight non-bending lines.[1] As a solution, an algebraic reconstruction algorithm such as SIRT is applied. This algorithm calculates the difference between measured and the calculated attenuation for the next projection and is mathematically expressed in the matrix formula below:

$$f_j^{(i)} = f_j^{(i-1)} - \frac{1}{M} \sum_{l=1}^{M} \frac{p_l^{(i-1)} - p_l}{\sum_k w_{lk}^2} w_{lj}$$

where f is the neutron attenuation coefficient, j is the cell number, i is the iteration step, p is the measured or computed ray-sum (projection), w_{lk} is the weight of k-cell corresponding to an l-ray.

SIRT can provide a more accurate representation thereby this study utilized this method for the reconstruction of the sample images.

The objective of this study is to identify the composition of a rock sample by 3D imaging techniques, comparison of the attenuation coefficient from a list of minerals, calculation of the volume fraction and production of a 3D image showing the different phases present in the rock sample.

2. Materials and Experimental setup

The rock sample used in this study was a heterogenous fragment of quartzite obtained from the collection of Institute of Geology of Ore Deposits, Petrography, Mineralogy and Geochemistry of the Russian Academy of Sciences (Fig. 1). Quartz of ferruginous quartzites are known to have alternating layers of quartz and iron oxides in which the genesis of such rocks originated through metasomatic transformation of primary biogenic limestones and the cyclic iron supply from deep-seated magmatic chamber (Zhabin & Sirotin, 2009).

The experiment was conducted in a specialized neutron radiography and tomography (NRT) facility at the high-flux IBR-2 reactor in Dubna, Russia. A block of the rock fragment, which is approximately 4.5 cm wide, was used in this experiment.
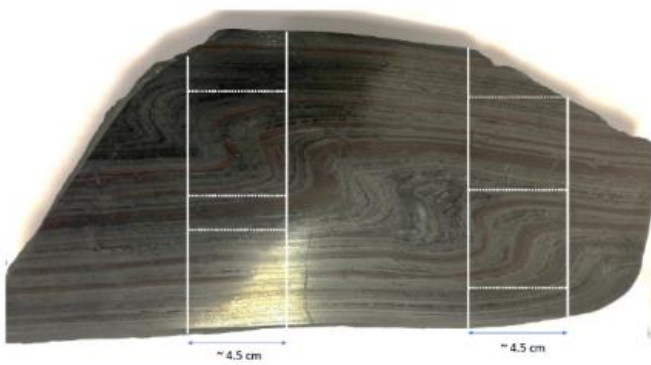

Figure 1. A photograph of the quartzite sample

Figure 2. The heterogenous quartzite rock sample on top of the turntable.

Table 1 summarized the technical parameters of the NRT facility. Figure 3 illustrated the schematic diagram of the experimental setup.
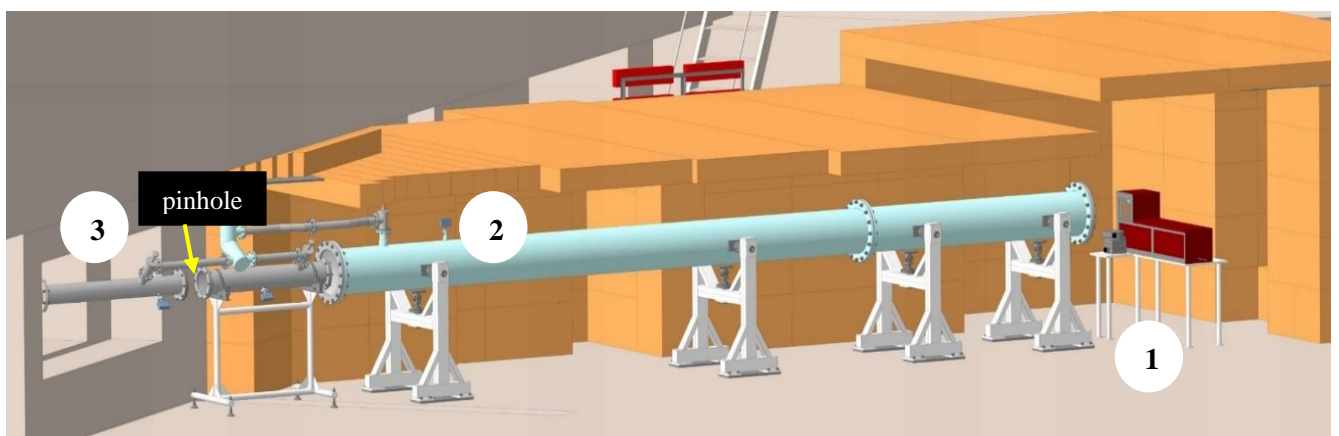

Figure 3. Schematic Diagram of the NRT Station at the IBR-2 Reactor in Dubna, Russia where (1) is the detector system, (2) is the collimation system and (3) is the neutron source.

Table 1.

Technical parameters of the NRT station in IBR-2 Reactor [4]

Parameter	
Characteristic collimation parameter L/D	200-2000
Size of input aperture of the collimation system D	5-50 mm
Distance between the system aperture and the sample position L	10 m
Size of neutron beam	20 x 20 cm^2
Characteristic parameter of the recording video camera	
Type of high sensitivity video camera	VIDEOSCAN-11002-2001
Size of the CCD matrix, pixels	2048 x 2048
Size of one pixel of the matrix, μm	9 x 9
Cooling	Peltier cooling to $-25℃$
Parameters of the optical system of the video camera	Based on Nikon objective with a focal distance of 50 mm and diaphragm width 1:1.4D

3. Results

3.1. Data pre-processing

The experimental data had three sets of images. The first set consists of the rock sample images taken at different angles; the second set consists of the dark field which accounts for the noise from the instrument while the third set consists of the open beam where only the neutron source is captured.

To improve the analysis of the images taken from the experiment, there is a need to undergo data pre-processing of the captured images in order to reduce noise and eliminate as many artifacts as possible. ImageJ, a powerful image processing tool, was used to produce the output of this step.

It may happen that in the data set, there are data points that are significantly different. In each of our data sets, we have to apply a median filter to remove unusual values that distort the analysis. The remove outliers function in ImageJ made this easier and in this study, the radius and threshold was set to 2.0 and 400, respectively.

Both the projected images and open beam were subtracted to the dark field to eliminate the noise from the instrument followed by the division of the projected images with the open beam and converted it into a 32-bit image. Necessary image corrections and math processes were done to obtain an output ready for the reconstruction step. The images were rotated by 1.25 to account for the correction of the positioning as shown in Figure 4.
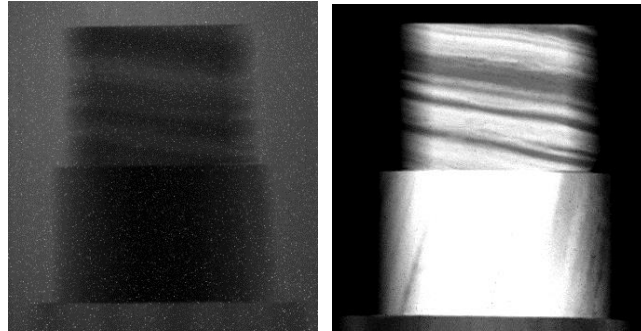

Figure 4. The projected image before pre-processing (left). The projected image after pre-processing (right) by adjusting brightness and contrast, applying median filter and subtracting the dark field.

3.2. Reconstruction and Rendering

Reconstruction is a mathematical process that generates tomographic images from a set of projected data taken at different angles. Image reconstruction was done using the SYRMEP Tomo Project (STP), an open-source software tool that allowed users to perform digital image processing easily. The images from pre-processing were saved as TIFF files because this file type can store color information and transparency of individual pixels.
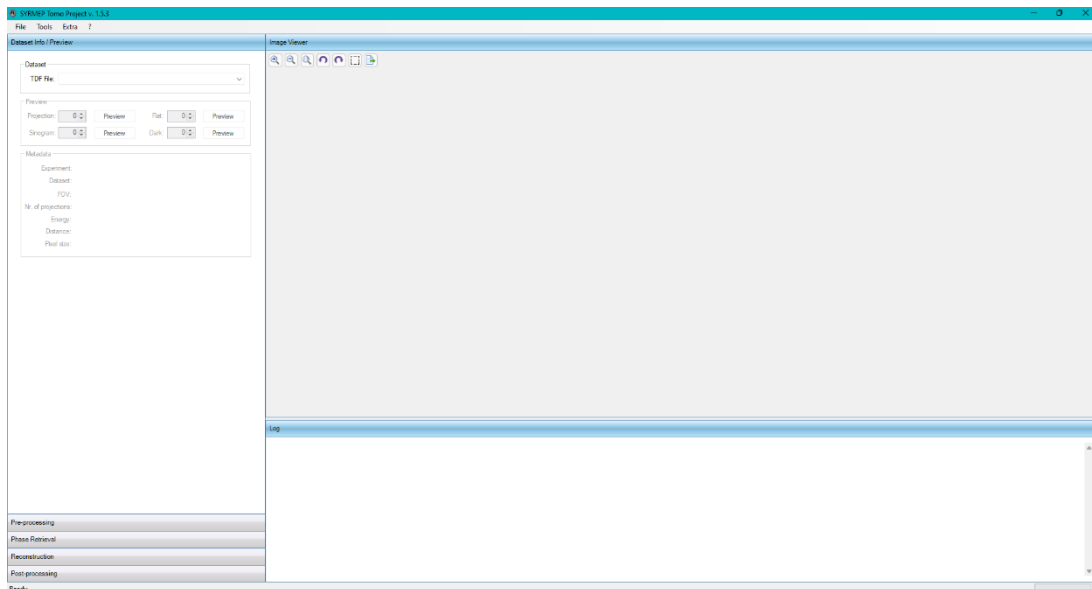

Figure 5. The user-friendly interface of the STP software where the pre-processing output in Fig. 3 was reconstructed.

The STP software has a convenient method of converting TIFF file types to TDF and further process the images in the de-stripping option. This option removed the ring artifacts and, in this study, the Oimoen, 2000 method was used with vertical and horizontal parameters of 31 and 71, respectively. Moreover, the STP software

7

determined the center of rotation of the image files which was set to 18. Two samples were reconstructed after hours of calculations using this software.
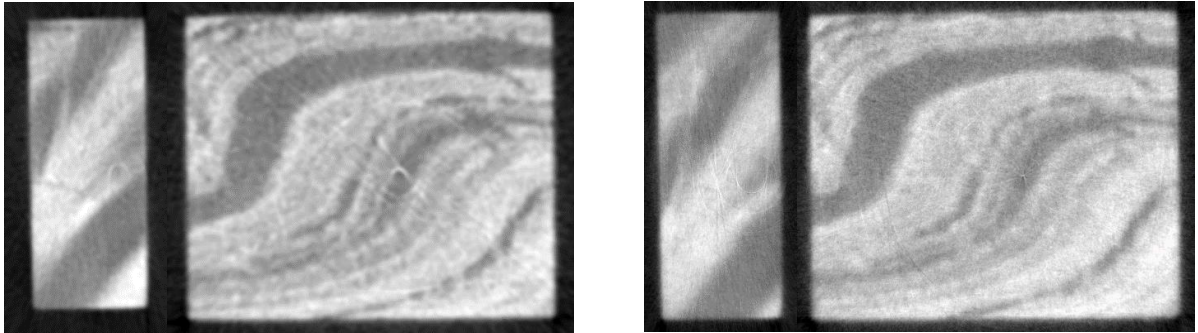

Figure 6. (Left) Reconstructed images using FBP algorithm with the application of the Shepp-Logan filter. (Right) Reconstructed images using SIRT algorithm with 100 iterations.

The reconstructed images using SIRT algorithm were utilized for the post-processing step because it had detailed look into the structure of the sample. There were two samples from the reconstructed images. For each sample, a volume of interest (VOI) was created. To do so, a binary image of the sample volume, also known as sample mask, was obtained by setting the appropriate threshold.

By using morphological erosion, the volume was cropped and the boundaries of the VOI are defined. The sample mask was divided by 255 and the original 32-bit slices was multiplied to the sample mask in order to get the "cropped" VOI. For 3D rendering, only the "cropped" data was used shown in Figure 7.
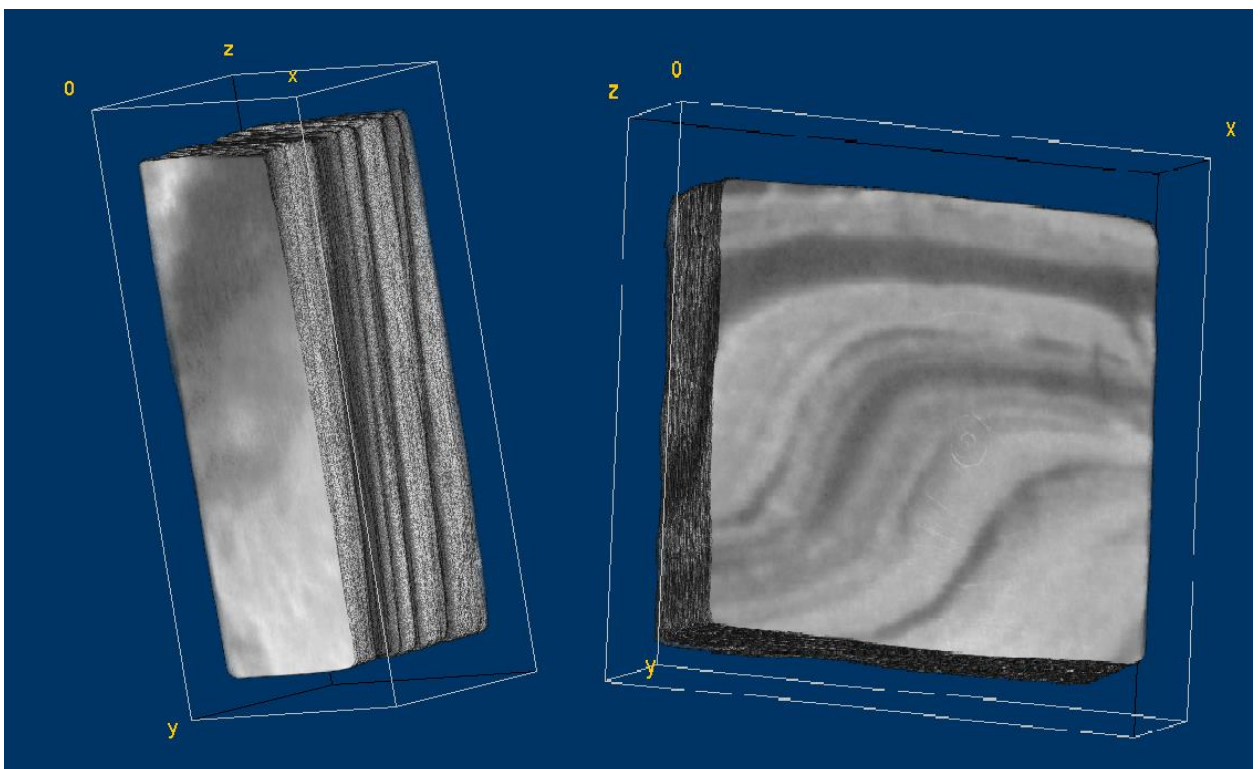

Figure 7. The rendered 3D models of the studied sample 1 (left) and sample (2) in 8-bit grayscale format.

For colored 32-bit images, this study used the recommended Green Fire Blue colormap. The image type was transformed to RGB 24-bit color before adjusting it to 8-bit color.
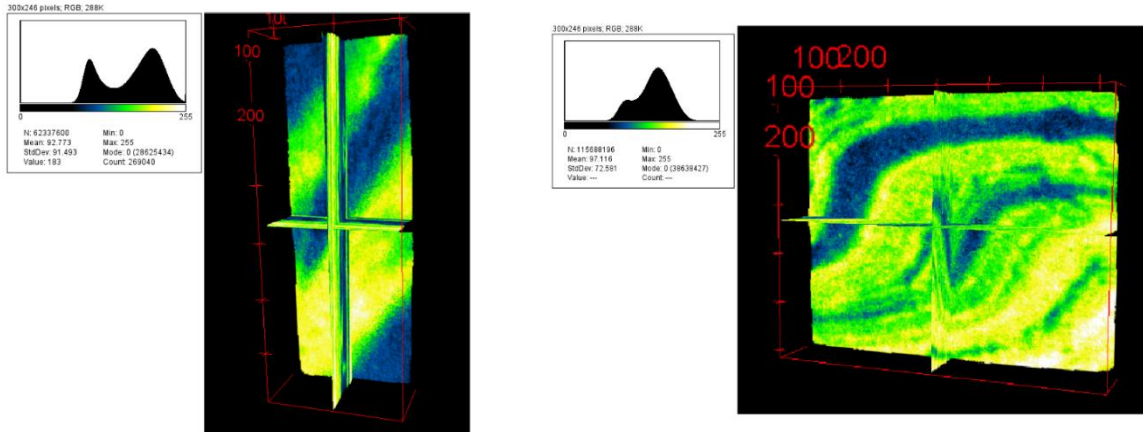

Figure 8. The rendered 3D models in orthogonal view of sample1 (left) and sample 2 (right) in Green Fire Blue colormap with their corresponding histogram profiles.

3.3. Post-processing step (3D data analysis)

The neutron attenuation coefficient is an important data that helped us in the determination of the phases present. Since the macroscopic cross section is related to the linear attenuation coefficient from Beer-Lambert Law, the data shown in Figure 9 was calculated based on the following general equation:

$$\mu = \frac{\rho}{M \times 1.66 \; x \; 10^{-27} \; kg} \; (\sigma) \; x \; 10^{-28} \; m^2$$

where ρ is the density, M is the molar mass, and σ is the total microscopic neutron cross section.
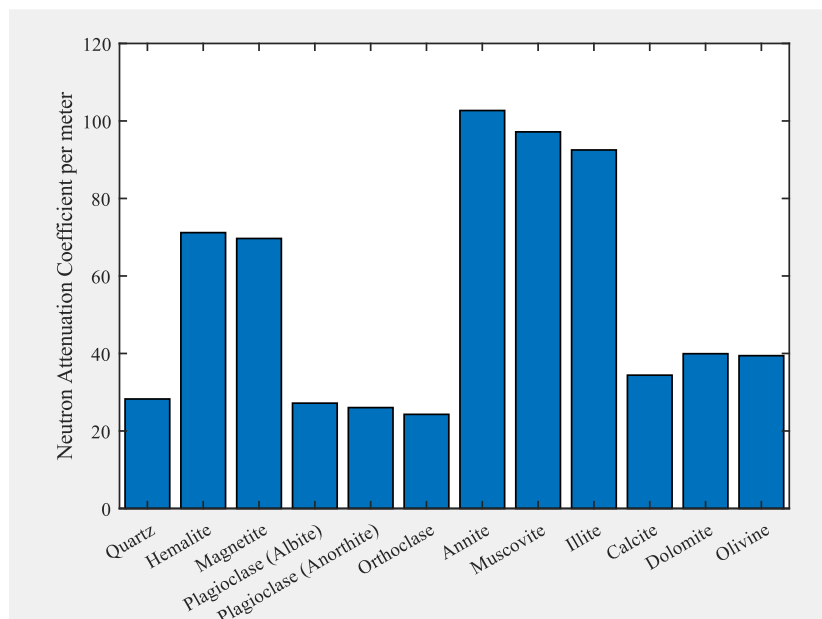

Figure 9. The list of common minerals with their computed neutron attenuation coefficient, m^{-1}

Though neutrons react weakly with most minerals, it can drastically affect the attenuation of a mineral if it contains elements with large cross section scattering such as hydrogen and iron. Based on the graph in Fig. 9, annite, muscovite and illite have high neutron attenuation coefficient per meter because they contain 2 hydrogen atoms.

Considering the studied rock sample, the iron-rich phase showed more attenuation with neutrons compared to the quartz-rich phase resulting to a higher peak in Figure 7.

Based on the rendered 3D models in Fig. 7 and Fig. 8, there can be two phases present and segmentation of the phases was necessary to further analyze the 3D data. By analyzing the stacked histogram of the two samples, the appropriate threshold was determined.
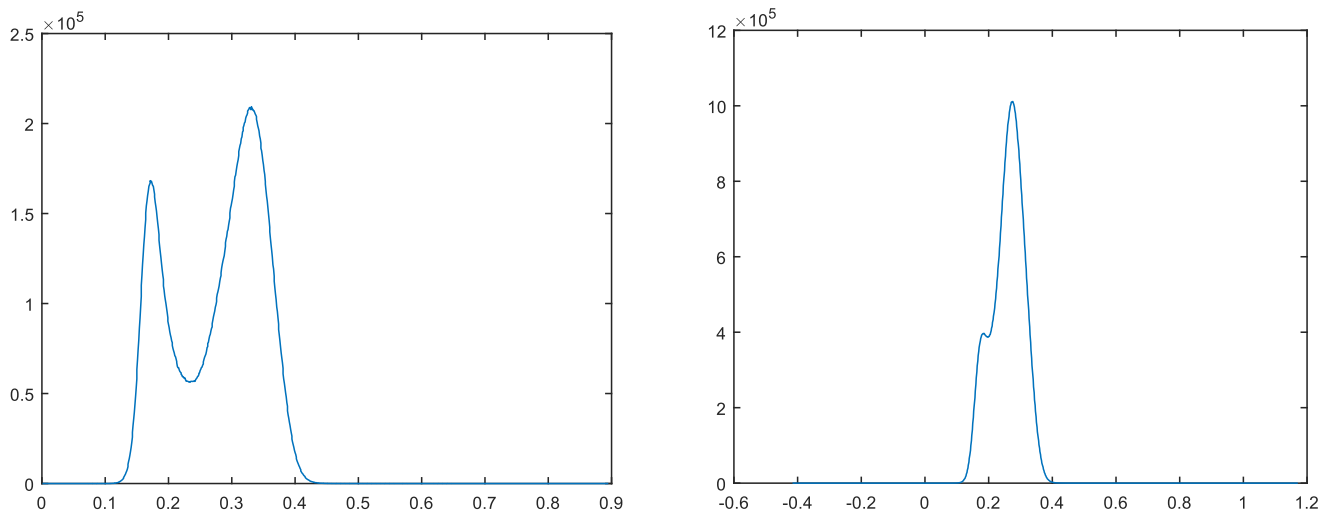

Figure 10. The histogram Plot of Sample 1 (left) and Sample 2 (right). Based on the two plots, two phases were present, the iron-rich phase and the quartz-rich phase.

For sample 1, the threshold for the iron-phase was at 0.24 and based on inspection of the graph in Figure 9, the two phases were clearly distinct. While for sample 2, there can be three phases: the iron-rich phase (threshold at 0.27), the mixture of iron and quartz phase (threshold between 0.22-0.27) and the quartz-rich phase (threshold at 0.22).
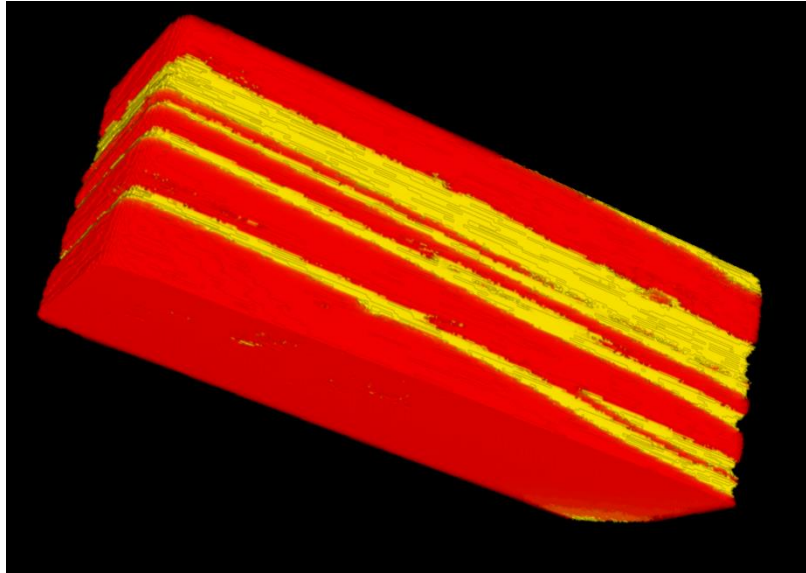
Figure 11. The rendered 3D model (Sample 1) of the studied heterogenous rock sample showing the two phases present: the iron-rich phase (red-colored part) and the quartz-rich phase (yellow-colored part).
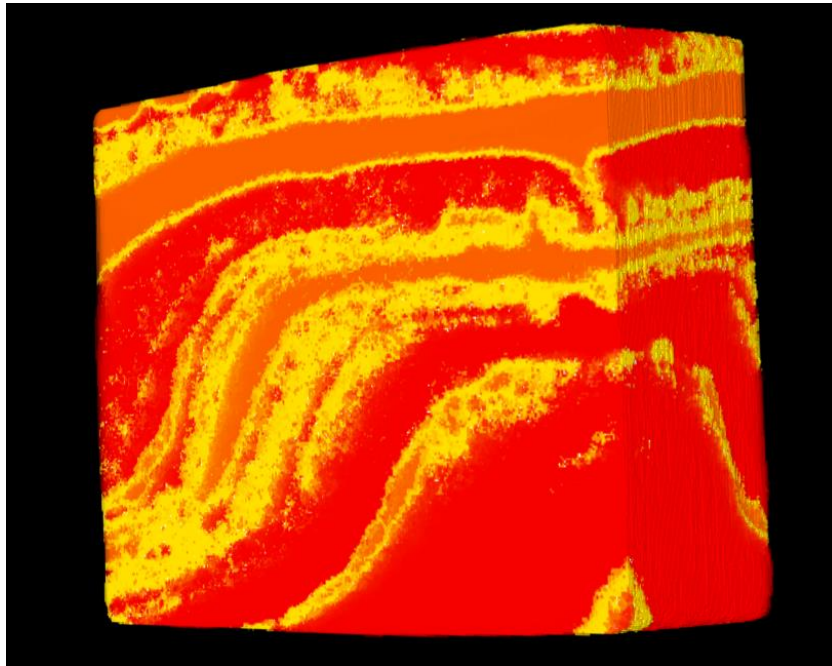

Figure 12. The rendered 3D model (Sample 2) of the studied heterogenous rock sample showing the three phases present: the iron-rich phase (red-colored part), the mixture of iron and quartz phase (yellow-colored part) and the quartz-rich phase (orange-colored part).

To determine the percentage of the phases, the ratio between the phase volume and sample volume was calculated. For sample 1, the binary image of the iron-rich phase was imported in ImageJ and the sum of the values in the slices was computed using the Z Project—a method that analyzes a stack by the application of various projection methods to the pixels within the stack. The measured mean value for the iron-rich phase in sample 1 was 21,720.161.

The same steps were followed for the sample 1 mask to obtain the mean value which represents the sample volume. These two values were necessary to compute for the volume fraction of phase expressed mathematically as:

$$volume\ fraction\ of\ phase = \frac{mean\ value\ of\ phase}{mean\ value\ of\ sample\ mask}\ x\ 100\%$$

The remaining percentage represents the other phase present in the sample. The phase fractions of the two samples were summarized in Table 2.

Table 2.

Phase Volume Fractions in Sample 1 and Sample 2

	Iron-Rich Phase (%)	Mixture (%)	Quartz-Rich Phase (%)
Sample 1	67.31	-	32.69
Sample 2	62.88	15.49	32.47

4. Conclusions

Neutron tomography allowed us to study the internal structure of a heterogenous rock without destructing the sample. The composition of the studied rock sample was found to contain approximately 65% iron-rich phase and 32% quartz-rich phase.

Image analysis can be a tricky process in obtaining the final 3D output. A number of factors greatly affected the data such as center of rotation, outliers, the different types of artifacts present in the images, the reconstruction algorithm and the computer system used in processing these images. If the computer system can't handle a lot of data processing, there is a need to reduce the file size which may provide a slight difference in the obtained result.

Despite the challenges, 3D imaging using neutrons is a promising nondestructive analytical tool in various fields to obtain valuable information about the inner structure with more accuracy and precision.

Acknowledgments

References

1. Andersen, A. (1984). Simultaneous algebraic reconstruction technique (SART): A superior implementation of the art algorithm. *Ultrasonic Imaging*, *6*(1), 81–94. https://doi.org/10.1016/0161-7346(84)90008-7
2. Brun, F., Massimi, L., Fratini, M., Dreossi, D., Billé, F., Accardo, A., Pugliese, R., & Cedola, A. (2017, January 19). *SYRMEP Tomo Project: A graphical user interface for customizing CT reconstruction workflows - advanced structural and chemical imaging*. SpringerOpen. Retrieved March 11, 2022, from https://ascimaging.springeropen.com/articles/10.1186/s40679-016-0036-8
3. Cleveland, T. E., Hussey, D. S., Chen, Z.-Y., Jacobson, D. L., Brown, R. L., Carter-Wientjes, C., Cleveland, T. E., & Arif, M. (2008). The use of neutron tomography for the structural analysis of corn kernels. *Journal of Cereal Science*, *48*(2), 517–525. https://doi.org/10.1016/j.jcs.2007.12.003
4. D. P. Kozlenko, "Neutron imaging facility at IBR-2 high flux pulsed reactor: first results," in Proceedings of the 10th World Conference on Neutron Radiography, Grindelwald, Switzerland, 2014, p. 27.
5. Kichanov, S. E., Kozlenko, D. P., Lukin, E. V., Rutkauskas, A. V., Krasavin, E. A., Rozanov, A. Y., & Savenko, B. N. (2018). A neutron tomography study of the Seymchan Pallasite. *Meteoritics & Planetary Science*, *53*(10), 2155–2164. https://doi.org/10.1111/maps.13115
6. Kichanov, S. E., Nazarov, K. M., Kozlenko, D. P., Saprykina, I. A., Lukin, E. V., & Savenko, B. N. (2017). Analysis of the internal structure of ancient copper coins by neutron tomography. *Journal of Surface Investigation: X-Ray, Synchrotron and Neutron Techniques*, *11*(3), 585–589. https://doi.org/10.1134/s1027451017030296
7. Kozlenko, D. P., Kichanov, S. E., Lukin, E. V., Rutkauskas, A. V., Belushkin, A. V., Bokuchava, G. D., & Savenko, B. N. (2016). Neutron radiography and tomography facility at IBR-2 Reactor. *Physics of Particles and Nuclei Letters*, *13*(3), 346–351. https://doi.org/10.1134/s1547477116030146
8. Research Reactor Data Base. Available online: https://nucleus.iaea.org/RRDB/RR/ (accessed on February 18 2022)
9. Squires, G. L. (2013). Basic Properties of the Neutron. In *Introduction to the theory of thermal neutron scattering*. essay, Cambridge University Press.
10. Zhabin, A. V., & Sirotin, V. I. (2009). Origin of ferruginous quartzites of the Kursk magnetic anomaly. *Doklady Earth Sciences*, *427*(1), 737–739. https://doi.org/10.1134/s1028334x09050079